NANO LETTERS

pubs.acs.org/NanoLett Letter

Dynamic Tuning of Moiré Excitons in a WSe_2/WS_2 Heterostructure via Mechanical Deformation

Wenyu Zhao, Emma C. Regan, Danqing Wang, Chenhao Jin, Satcher Hsieh, Zhiyuan Wang, Jialu Wang, Zilin Wang, Kentaro Yumigeta, Mark Blei, Kenji Watanabe, Takashi Taniguchi, Sefaattin Tongay, Norman Y. Yao, and Feng Wang*

Cite This: *Nano Lett.* 2021, 21, 8910–8916 Read Online

ACCESS | Metrics & More | Article Recommendations | Supporting Information

ABSTRACT: Moiré superlattices in van der Waals (vdW) heterostructures form by stacking atomically thin layers on top of one another with a twist angle or lattice mismatch. The resulting moiré potential leads to a strong modification of the band structure, which can give rise to exotic quantum phenomena ranging from correlated insulators and superconductors to moiré excitons and Wigner crystals. Here, we demonstrate the dynamic tuning of moiré potential in a WSe_2/WS_2 heterostructure at cryogenic temperature. We utilize the optical fiber tip of a cryogenic scanning near-field optical microscope (SNOM) to locally deform the heterostructure and measure its near-field optical response simultaneously. The deformation of the heterostructure increases the moiré potential, which leads to a red shift of the moiré exciton resonances. We observe the interlayer exciton resonance shifts up to 20 meV, while the intralayer exciton resonances shift up to 17 meV.

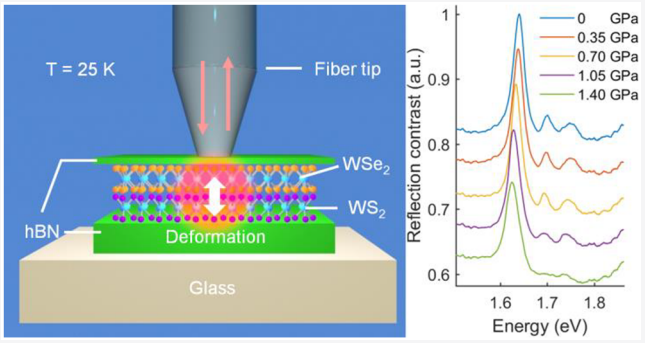

KEYWORDS: *Moiré exciton, Cryogenic near-field nanoscopy, Nanoindentation*

INTRODUCTION

Moiré superlattices in van der Waals (vdW) heterostructures have become a playground of exotic quantum phenomena due to the interplay between atomic structure and electron correlations.[1−15] The long-wavelength moiré potential, generated by the twist angle and lattice mismatch between the constitutive layers, leads to a strong modification of the band structure and gives rise to a number of emergent electronic phenomena including superconductivity,[3,5] magnetism,[16] fractional Chern insulating states,[17] and moiré excitons.[18−23] Dynamic control of the moiré potential in situ is highly desirable in the study of moiré physics. One promising way is through mechanical deformation, which directly alters the interlayer separation of the heterostructures and therefore modulates the moiré potential and correlated states.[24−29] However, experimental realization of in situ deformation engineering of moiré heterostructures at low temperature has been difficult using conventional diamond anvil cell or piston−cylinder methods.[29]

Here, we demonstrate a novel way to locally deform vdW heterostructures in situ using an optical fiber tip in a cryogenic SNOM. The tapered optical fiber tip is used both to indent the vdW heterostructure and measure its near-field optical response simultaneously. Because of the highly confined optical field at the fiber tip, the measured spectra are dominated by the area directly below the tip where indentation occurs. We demonstrate efficient tuning of the moiré exciton peaks in WSe_2/WS_2 heterostructures, where the interlayer and intralayer moiré excitons can shift up to 20 and 17 meV, respectively. Our observations are well-captured by a phenomenological model which accounts for the deformation-induced increase of the moiré potential.

RESULTS AND DISCUSSION

Figure 1a illustrates our experimental design for the deformation tuning of moiré excitons in a WSe_2/WS_2 heterostructure. A tapered optical fiber of a SNOM serves both to indent the sample and perform optical spectroscopy in reflection mode. The excitation light is coupled into the fiber and propagates to the tapered tip. The reflected light is then coupled back into the tip and backpropagates to a spectrometer. The local stress below the tip can be calibrated

Received: September 16, 2021
Revised: October 12, 2021
Published: October 18, 2021

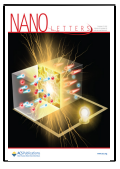

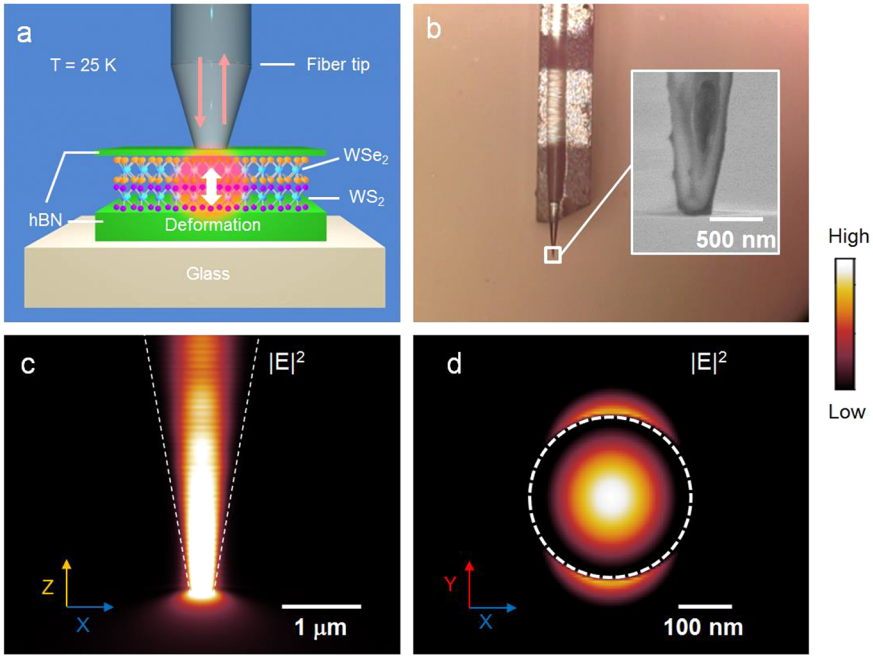

Figure 1. Dynamic tuning of moiré excitons in WSe_2/WS_2 heterostructure using an optical fiber tip. (a) Schematic view of the dynamic tuning of moiré excitons in WSe_2/WS_2 heterostructure. The optical fiber tip is used both to indent the heterostructure and probe its optical near-field response. (b) Optical image of the etched fiber tip after being glued onto the tuning fork. The inset shows a scanning electron micrograph of the tip. The tip end has a diameter of ∼300 nm. (c) Simulated field distribution along the fiber tip for HeNe laser. The tip contour is indicated by white dashed lines. The light can be focused down to a submicron spot defined by the tip size. (d) Simulated field distribution of the cross-section at the tip end. The light is mainly confined inside the optical fiber tip.

by comparing to a separate experiment performed in a diamond anvil cell.

The tapered optical fiber is etched from a single mode optical fiber (780 HP) using hydrofluoric acid (HF) following procedures described in ref 30 and 31 (see Methods for details). The tapered tip with a diameter of ∼300 nm is then glued onto a tuning fork leg as shown in Figure 1b. In order to retain a rigid tip, we restrict the tuning fork leg from protruding less than 0.2 mm. The tuning fork with the tip is installed into a home-built cryogenic SNOM that operates at a base temperature of 25 K. The SNOM operates in a shear-force mode in which the tuning fork with the tip vibrates at its mechanical resonance frequency near 32 kHz through a self-excitation loop.[32,33] The mechanical resonance frequency shifts significantly as the tip approaches the sample. By monitoring this frequency shift, the tip−sample distance can be accurately controlled to within a few nanometers.[32,33] After the tip reaches a distance of ∼5 nm[34,35] above the sample surface, the feedback is temporarily turned off, and the applied stress can be controlled by the compressive displacement of the sample relative to the tip using a piezo stage. The compressive displacement is calibrated by scanning a known calibration grating at cryogenic temperature. The voltage driving the piezo tube can then be correlated to the height of the sample.

Our method of using a fiber tip to apply stress is distinct from conventional diamond anvil cell (DAC) measurements[20,21] and possesses unique advantages. First, the stress can be easily and continuously varied in situ with high precision. Although in situ control of pressure can be realized in specially designed DACs,[36−38] integrating such tunable DACs with cryogenic optical measurements introduces significant technical challenges. Second, local spectroscopy with submicron spatial resolution can be carried out using the SNOM while applying stress with the tip, which minimizes the effect of sample inhomogeneity in spectroscopy measurements.

We perform either photoluminescence (PL) or reflection spectroscopy using fiber-coupled HeNe and supercontinuum lasers, respectively. In PL spectroscopy, the PL emission from the sample is collected by a spectrometer equipped with a cooled CCD camera. In reflection spectroscopy, the analogous procedure occurs for the reflected light from the sample. Figure 1c shows the simulated electric field distribution of the excitation light propagating along the tapered tip using a HeNe laser. The fiber contour is indicated by white dashed lines. The excitation light can be efficiently confined within the optical fiber and focused down to a submicron spot determined by the tip geometry. Figure 1d shows the field distribution at the tip end. The light is largely confined inside the fiber tip with only 9% leaked outside. The strong field confinement ensures that only the deformed area directly below the fiber tip contributes to the measured optical response.

Figure 2a shows an optical image of a representative WSe_2/WS_2 heterostructure. The heterostructure is encapsulated by two hexagonal boron nitride (hBN) flakes using a dry-transfer technique. All of the 2D materials in our experiment are first mechanically exfoliated from bulk crystals, stacked together using a propylene carbonate (PPC) stamp, and placed on a transparent sapphire substrate (see Methods for details). After encapsulation, the optical contrast of the WSe_2/WS_2 layers becomes weak; for reference, Figure 2a inset shows the same flakes on a 285 nm SiO_2/Si substrate before transfer. The relative twist angle between the WSe_2 and WS_2 layers is determined optically using polarization-dependent second-harmonic-generation measurements. The fitted data (Figure 2b) indicates that the heterostructure has a nearly zero twist angle ($0.7 \pm 0.3°$) between the WSe_2 and WS_2 flakes.

https://doi.org/10.1021/acs.nanolett.1c03611
Nano Lett. 2021, 21, 8910−8916

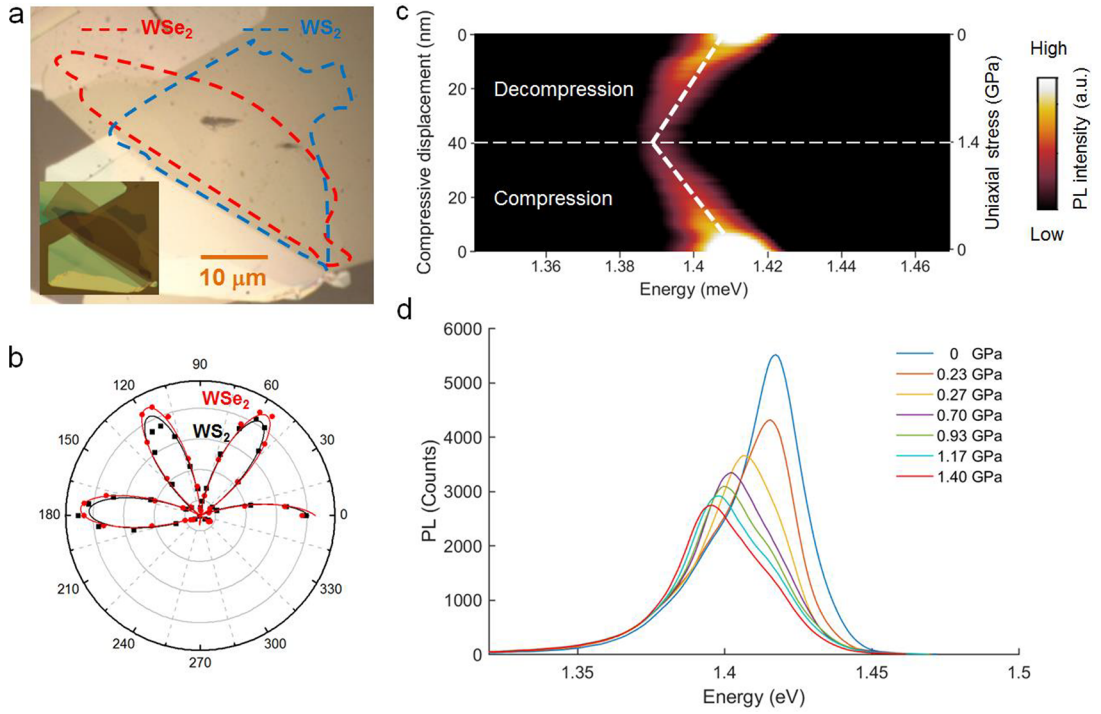

Figure 2. Experimental results of moiré interlayer excitons in WSe_2/WS_2 heterostructure under applied stress. (a) Optical image of a hBN-encapsulated WSe_2/WS_2 heterostructure placed on a transparent sapphire substrate. The WSe_2 is indicated by the red dashed line and the WS_2 is indicated by the blue dashed line. The inset shows the optical image of the heterostructure on a 285 nm SiO_2/Si substrate prior to transfer. (b) Second-harmonic generation of the WSe_2 and WS_2 monolayer regions within the heterostructure. The fitted twist angle between the two layers is $0.7 \pm 0.3°$ indicating a nearly zero twist angle of the sample. (c) PL spectra of the moiré interlayer exciton evolution under applied stress. The resonance shifts to lower energies upon compression and shows negligible hysteresis upon decompression. The frequency modulation feedback is used to control the fiber tip to reach the sample surface. Then the feedback is temporarily turned off and the fiber tip is intended into the sample by controlling the compressive displacement from 0 to 40 nm. After the tip is intended into the sample by 40 nm, the tip is gradually retracted with compressive displacement reducing from 40 to 0 nm. (d) Horizontal line cuts of c showing the WSe_2/WS_2 PL spectra at selected applied stresses.

We first measure the deformation-induced change of the interlayer exciton in the WS_2/WSe_2 heterostructure using near-field photoluminescence spectroscopy. Figure 2c shows the PL spectra of the WSe_2/WS_2 heterostructure as a function of the compressive displacement, wherein the sample is compressed and subsequently decompressed. At zero applied stress, the PL spectra show a well-defined peak at 1.41 eV, corresponding to emission from the lowest-energy interlayer exciton state in the heterostructure.[18,39] The WSe_2/WS_2 heterostructure has a type II band alignment, so interlayer excitons form with a hole layer in WSe_2 and an electron layer in WS_2.[40] Because of the spatial separation of the charge carriers, the oscillator strength of this interlayer exciton is considerably smaller than that of intralayer ones, yet they dominate the emission due to their long lifetimes.[18,22] As we increase the applied stress, the interlayer exciton exhibits a continuous red shift that scales approximately linearly. Figure 2d shows the PL spectra of the interlayer exciton at several selected applied stresses from horizontal line cuts in Figure 2c. The PL spectrum exhibits a well-defined peak even at the maximum applied stress. The resonance energy is red-shifted by 20 meV at the highest applied stress, accompanied by a reduction in the overall emission intensity.

We calibrate the stress exerted by the fiber tip by comparing the deformation-induced interlayer exciton shift in the WS_2/WSe_2 moiré heterostructure to that measured in a diamond anvil cell. In the diamond anvil cell measurement, we place the WS_2/WSe_2 heterostructure onto the culet (tip) of a diamond anvil and compress it with an opposing anvil using a 4:1 methanol/ethanol mixture as a pressure-transmitting medium. The pressure within the medium is measured using the PL shift of a ruby microsphere placed near the heterostructure; this measurement also characterizes the uniaxial stress applied to the sample[41] (see SI for details). We compress the cell at room temperature and subsequently cool it to 25 K in the cryostat. The PL spectra for both the heterostructure and the ruby microsphere are obtained through a long-working-distance objective lens. We observe a red shift of the interlayer moiré exciton under compression and obtain a stress-induced exciton energy shift of 14.3 meV/GPa. In our SNOM measurements, the interlayer exciton shifts linearly with the compressive displacement with a slope of 0.5 meV/nm. Comparison of these two sets of data shows that the tip-induced deformation increases linearly with the compressive displacement at a rate of 0.035 GPa/nm. The largest compressive displacement applied in our measurements is 40 nm, which corresponds to a local uniaxial stress of 1.4 GPa. This maximum stress is limited by the damage threshold of the optical fiber tip and can potentially be increased by using a tip made from stronger materials.

Next we examine the deformation-induced modification of the intralayer moiré excitons in the WS_2/WSe_2 heterostructure. Figure 3a shows the measured reflection contrast of the WSe_2/WS_2 heterostructure as a function of the stress applied by the optical fiber tip. The high energy peaks of the moiré excitons are rescaled for visual clarity. Figure 3b shows the reflection spectra at several selected applied stresses, which are horizontal line cuts of Figure 3a. In the absence of any compression, the

https://doi.org/10.1021/acs.nanolett.1c03611
Nano Lett. 2021, 21, 8910−8916

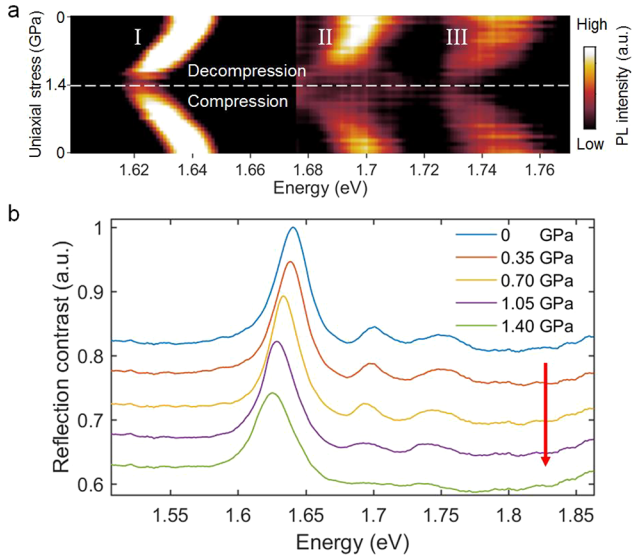

Figure 3. Experimental results of moiré intralayer excitons in WSe_2/WS_2 heterostructure under applied stress. (a) Optical reflection contrast of the WSe_2 moiré A excitons under applied stress. The optical spectra show negligible hysteresis in the compression and decompression traces. (b) Horizontal line cuts show the reflection contrast spectra of the intralayer moiré A excitons of the WSe_2. The moiré exciton peaks exhibit red shifts and line width broadening upon compression.

heterostructure shows three distinct peaks (I, II, III) at 1.641 eV, 1.701 and 1.752 eV, respectively, corresponding to the moiré excitons resulting from the periodic moiré potential in the WS_2/WSe_2 heterostructure.[42] All three peaks exhibit a red shift of their transition energies with increased stress. This red shift in energy is accompanied by lower contrast and line width broadening, particularly for the II and III moiré exciton peaks. At the maximum stress (1.4 GPa), only I and III peaks show well-defined absorption resonances. The red shift in moiré exciton energies shows the same behavior in compression and decompression traces with negligible hysteresis, and the moiré excitons fully recover to their original positions when the fiber tip is released. The measurement is highly reproducible, and neither the tip nor the sample show signs of degradation after a compression−decompression cycle.

To understand this stress-induced red shift of the intralayer moiré exciton resonances, we perform control measurements of isolated WSe_2 monolayers encapsulated in hBN. We find that the 1s exciton of the isolated WSe_2 monolayer shows negligible red shift under the same experimental conditions (See SI for details), suggesting that the red shift of the moiré exciton resonances arises from a stress-induced modulation of the moiré potential in the WS_2/WSe_2 heterostructure. To elucidate this effect, we construct a phenomenological model following ref 42. The center-of-mass motion of WSe_2 A excitons can be described by the Hamiltonian[42]

$$H = H_0 + \sum_{j=1}^{6} V_j \exp(i\mathbf{b}_j \cdot \mathbf{r})$$

where H_0 is the low-energy effective Hamiltonian for the A exciton 1s state in monolayer WSe_2. V_j is the effective potential coefficient on the exciton generated by the moiré superlattices; its momentum is given by the reciprocal lattice vectors of the moiré superlattices, $\mathbf{b}_j$. Here, only one component in V_j is independent due to the 3-fold rotational symmetry and hermiticity. The effective moiré potential coefficient can then be defined as $V_1 = V \exp(i\psi)$ in which V and ψ are the amplitude and phase components, respectively.[42] We note that the peak-to-peak value of the moiré potential is nearly an order of magnitude larger than V. Figure 4a,b shows the exciton dispersion in the mini-Brillouin zone under different moiré potentials calculated from this model. γ, m, and κ are the high

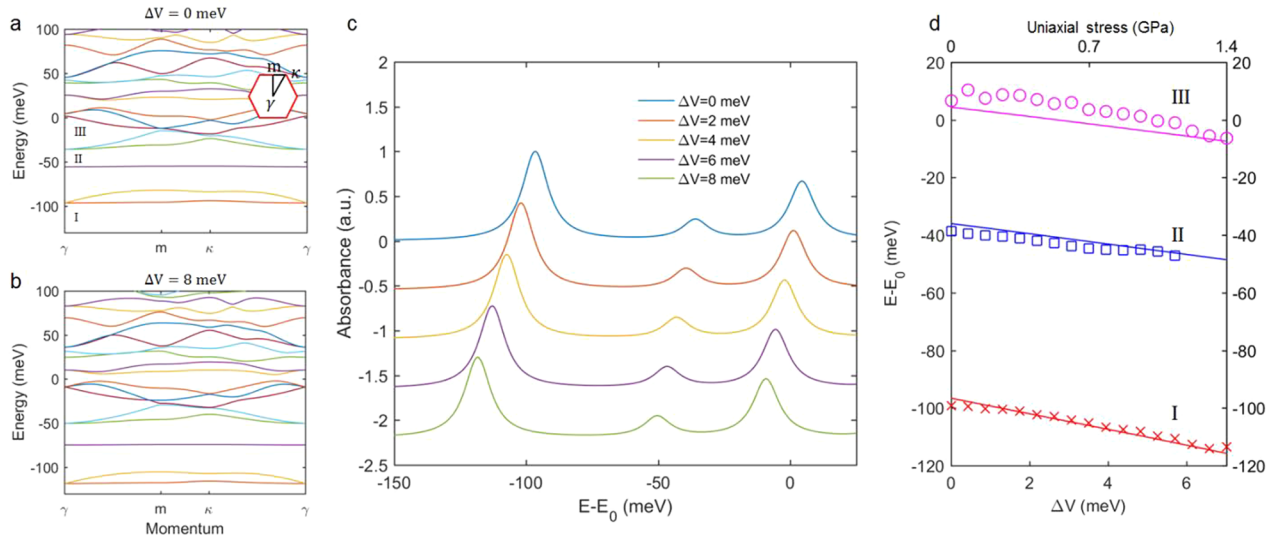

Figure 4. Calculated moiré exciton shift in WSe_2/WS_2 heterostructure. WSe_2 A exciton dispersion in the mini-Brillouin zone with a moiré potential modulation of (a) ΔV = 0 meV and (b) ΔV = 8 meV. The original moiré potential parameters are V = 54 meV, ψ = 15°. The band structure in mini-Brillouin is very sensitive to the moiré potential. (c) Simulated optical absorption spectra of the intralayer moiré exciton at different moiré potentials. The absorption peaks shift to lower energy with increasing moiré potential. (d) Resonance energy shift of the moiré intralayer excitons extracted from the experimental data (markers) and compared with theoretical calculations (solid lines). The theory agrees well with the experiment observation when the moiré potential modulation reaches 7 meV. The three intralayer moiré exciton peaks all shift to lower energy with increased moiré potential, but they exhibit a slightly different slope: 2.63 for peak I, 1.83 for peak II, and 1.70 for peak III.

https://doi.org/10.1021/acs.nanolett.1c03611
Nano Lett. 2021, 21, 8910−8916

symmetry points of the mini-Brillouin zone (Figure 4a inset). A larger moiré potential that corresponds to the strong-coupling regime substantially modifies the exciton dispersion (Figure 4a and b). The energy of the moiré exciton states in different minibands (labeled I to III in Figure 4a) is highly sensitive to the moiré potential. This is also reflected in the simulated absorption spectrum as shown in Figure 4c. The energies of the corresponding absorption peaks red shift as the moiré potential increases. Figure 4d shows the calculated energy shift of the moiré intralayer exciton under applied stress compared to the experimental data. The calculated shift captures the experimental findings well with the largest red shift at a stress of 1.4 GPa corresponding to a 7 meV modulation of the moiré potential coefficient. The corresponding change of the peak-to-peak moiré potential is 70 meV.

CONCLUSION

In summary, we have demonstrated a novel way to dynamically tune moiré excitons in a WSe_2/WS_2 heterostructure. The sharp tip of a cryogenic SNOM allows us to apply mechanical stress and perform background-free near-field spectroscopy simultaneously. We observe a red shift of both the intralayer and interlayer excitons which corresponds to a deformation-induced modulation of the moiré potential coefficient by 7 meV. Our study of moiré excitons under deformation can be extended to other 2D materials such as twisted graphene and graphene-hBN superlattices, opening the door to electronic and optical studies of deformed 2D materials.

METHODS

Devices Preparation. Monolayer WSe_2, monolayer WS_2, and thin hBN flakes were exfoliated onto silicon substrates with a 285 nm SiO_2 layer. We then used a PPC stamp to pick up the bottom hBN flake, the WSe_2 monolayer, the WS_2 monolayer, and the top hBN flake in sequence. The angle of the PPC stamp was adjusted between picking up the WSe_2 and the WS_2 to ensure a near-zero twist angle between the flakes. Polarization-dependent second-harmonic generation was used to determine the relative angle between the WSe_2 and WS_2 flakes. In order to maintain an ultraclean surface, the PPC stamp with the heterostructure was then flipped over and stamped onto a sapphire substrate.

Chemical Etching of Optical Fiber Tips. A single mode optical fiber, 780HP from Thorlabs Inc., is immersed into an aqueous 54% HF solution with its acrylate jacket. The HF solution is covered by toluene to avoid acid evaporation. The acid diffuses through the acrylate jacket and etches the glass fiber. Because of the nonuniform etching speed, after 2 h a well-defined fiber tip forms. The tip is then dipped into acetone to remove the acrylate jacket.

Cryogenic SNOM for Optical Measurement under Deformation. Our cryogenic optical measurements were carried out on a tuning fork-based SNOM which can operate at high vacuum and cryogenic temperatures. The lowest sample temperature achieved in our measurements is 25 K. An optical fiber tip is fixed onto one of the tuning fork legs to detect the force between the tip and sample, which is a standard way to control the tip−sample distance. After the tip−sample distance reaches ∼5 nm, the feedback of the SNOM is temporarily tuned off, and the applied stress can be controlled by the height of the sample via a piezo stage. A compressive displacement of the sample toward the tip will increase the local stress on the tip−sample area. For the reflection contrast measurements, a supercontinuum laser is coupled into the fiber tip and the backpropagating light is sent to the spectrometer. During the measurement, the turbo pump is turned off in order to minimize mechanical vibrations. The background vacuum level remains below 1×10^{-6} mbar through all the measurements.

ASSOCIATED CONTENT

Supporting Information

The Supporting Information is available free of charge at https://pubs.acs.org/doi/10.1021/acs.nanolett.1c03611.

Calibration of the stress applied by the optical fiber tip and monolayer WSe_2 energy shift under applied deformation (PDF)

AUTHOR INFORMATION

Corresponding Author

Feng Wang − *Department of Physics, University of California at Berkeley, Berkeley, California 94720, United States; Materials Science Division, Lawrence Berkeley National Laboratory, Berkeley 94720 California, United States; Kavli Energy NanoSciences Institute at University of California Berkeley and Lawrence Berkeley National Laboratory, Berkeley, California 94720, United States*; Email: fengwang76@berkeley.edu

Authors

Wenyu Zhao − *Department of Physics, University of California at Berkeley, Berkeley, California 94720, United States*; orcid.org/0000-0001-5740-5613

Emma C. Regan − *Department of Physics and Graduate Group in Applied Science and Technology, University of California at Berkeley, Berkeley, California 94720, United States; Materials Science Division, Lawrence Berkeley National Laboratory, Berkeley 94720 California, United States*

Danqing Wang − *Department of Physics and Graduate Group in Applied Science and Technology, University of California at Berkeley, Berkeley, California 94720, United States; Materials Science Division, Lawrence Berkeley National Laboratory, Berkeley 94720 California, United States*

Chenhao Jin − *Kavli Institute at Cornell for Nanoscale Science, Ithaca, New York 14853, United States*

Satcher Hsieh − *Department of Physics, University of California at Berkeley, Berkeley, California 94720, United States; Materials Science Division, Lawrence Berkeley National Laboratory, Berkeley 94720 California, United States*

Zhiyuan Wang − *Department of Physics, University of California at Berkeley, Berkeley, California 94720, United States*

Jialu Wang − *Department of Physics, University of California at Berkeley, Berkeley, California 94720, United States*

Zilin Wang − *Department of Physics, University of California at Berkeley, Berkeley, California 94720, United States*

Kentaro Yumigeta − *School for Engineering of Matter, Transport and Energy, Arizona State University, Tempe, Arizona 85287, United States*

Mark Blei − *School for Engineering of Matter, Transport and Energy, Arizona State University, Tempe, Arizona 85287, United States*

https://doi.org/10.1021/acs.nanolett.1c03611
Nano Lett. 2021, 21, 8910−8916

Kenji Watanabe − *Research Center for Functional Materials, National Institute for Materials Science, Tsukuba 305-0044, Japan;* orcid.org/0000-0003-3701-8119

Takashi Taniguchi − *International Center for Materials Nanoarchitectonics, National Institute for Materials Science, Tsukuba 305-0044, Japan;* orcid.org/0000-0002-1467-3105

Sefaattin Tongay − *School for Engineering of Matter, Transport and Energy, Arizona State University, Tempe, Arizona 85287, United States;* orcid.org/0000-0001-8294-984X

Norman Y. Yao − *Department of Physics, University of California at Berkeley, Berkeley, California 94720, United States; Materials Science Division, Lawrence Berkeley National Laboratory, Berkeley 94720 California, United States*

Complete contact information is available at: https://pubs.acs.org/10.1021/acs.nanolett.1c03611

Author Contributions

F.W. and N.Y.Y. conceived the research. W.Z. carried out cryogenic near-field optical measurements. E.R performed the polarization-dependent second-harmonic-generation measurements. W.Z. and S.H. prepared the diamond anvil cell measurements W.Z., E.R., D.W., Z.W., J.L., and Z.W. fabricated the heterostructure devices. W.Z., C.J., S.H., and F.W. performed data analysis. S.T, K.Y, and M.B grew flux zone growth crystals. K.W. and T.T. grew hexagonal boron nitride crystals. All authors discussed the results and wrote the manuscript.

Notes

The authors declare no competing financial interest.

■ ACKNOWLEDGMENTS

This work was supported primarily by the Director, Office of Science, Office of Basic Energy Sciences, Materials Sciences and Engineering Division of the U.S. Department of Energy under contract number DE-AC02-05CH11231 (van der Waals heterostructures program, KCWF16). This device fabrication was supported by the Office of Naval research (MURI award N00014-16-1-2921). S.T acknowledges the use of facilities within the Eyring Materials Center at Arizona State University supported in part by NNCI-ECCS-1542160. S.T acknowledges support from DOE-SC0020653, NSF CMMI 1933214, NSF DMR 1552220, and DMR 1955889. K.W. and T.T. acknowledge support from the Elemental Strategy Initiative conducted by the MEXT, Japan, Grant JPMXP0112101001, JSPS KAKENHI Grant JP20H00354, and the CREST(JPMJCR15F3), JST. E.C.R. acknowledges support from the Department of Defense through the National Defense Science and Engineering Graduate Fellowship (NDSEG) Program.

■ REFERENCES

(1) Abbas, G.; Li, Y.; Wang, H.; Zhang, W. X.; Wang, C.; Zhang, H. Recent advances in twisted structures of flatland materials and crafting Moire superlattices. *Adv. Funct. Mater.* **2020**, *30* (36), 2000878.

(2) Cao, Y.; Fatemi, V.; Demir, A.; Fang, S.; Tomarken, S. L.; Luo, J. Y.; Sanchez-Yamagishi, J. D.; Watanabe, K.; Taniguchi, T.; Kaxiras, E.; Ashoori, R. C.; Jarillo-Herrero, P. Correlated insulator behaviour at half-filling in magic-angle graphene superlattices. *Nature* **2018**, *556* (7699), 80−84.

(3) Cao, Y.; Fatemi, V.; Fang, S.; Watanabe, K.; Taniguchi, T.; Kaxiras, E.; Jarillo-Herrero, P. Unconventional superconductivity in magic-angle graphene superlattices. *Nature* **2018**, *556* (7699), 43−50.

(4) Chen, G.; Jiang, L.; Wu, S.; Lyu, B.; Li, H.; Chittari, B. L.; Watanabe, K.; Taniguchi, T.; Shi, Z.; Jung, J.; Zhang, Y.; Wang, F. Evidence of a gate-tunable Mott insulator in a trilayer graphene moiré superlattice. *Nat. Phys.* **2019**, *15* (3), 237−241.

(5) Chen, G.; Sharpe, A. L.; Gallagher, P.; Rosen, I. T.; Fox, E. J.; Jiang, L.; Lyu, B.; Li, H.; Watanabe, K.; Taniguchi, T.; Jung, J.; Shi, Z.; Goldhaber-Gordon, D.; Zhang, Y.; Wang, F. Signatures of tunable superconductivity in a trilayer graphene moiré superlattice. *Nature* **2019**, *572* (7768), 215−219.

(6) Choi, Y.; Kemmer, J.; Peng, Y.; Thomson, A.; Arora, H.; Polski, R.; Zhang, Y.; Ren, H.; Alicea, J.; Refael, G.; von Oppen, F.; Watanabe, K.; Taniguchi, T.; Nadj-Perge, S. Electronic correlations in twisted bilayer graphene near the magic angle. *Nat. Phys.* **2019**, *15* (11), 1174−1180.

(7) Zheng, Z.; Ma, Q.; Bi, Z.; de la Barrera, S.; Liu, M.-H.; Mao, N.; Zhang, Y.; Kiper, N.; Watanabe, K.; Taniguchi, T.; Kong, J.; Tisdale, W. A.; Ashoori, R.; Gedik, N.; Fu, L.; Xu, S.-Y.; Jarillo-Herrero, P. Unconventional ferroelectricity in moiré heterostructures. *Nature* **2020**, *588*, 1−6.

(8) Regan, E. C.; Wang, D.; Jin, C.; Bakti Utama, M. I.; Gao, B.; Wei, X.; Zhao, S.; Zhao, W.; Zhang, Z.; Yumigeta, K.; Blei, M.; Carlstrom, J. D.; Watanabe, K.; Taniguchi, T.; Tongay, S.; Crommie, M.; Zettl, A.; Wang, F. Mott and generalized Wigner crystal states in WSe 2/WS 2 moiré superlattices. *Nature* **2020**, *579* (7799), 359−363.

(9) Shimazaki, Y.; Schwartz, I.; Watanabe, K.; Taniguchi, T.; Kroner, M.; Imamoğlu, A. Strongly correlated electrons and hybrid excitons in a moiré heterostructure. *Nature* **2020**, *580* (7804), 472−477.

(10) Tang, Y.; Li, L.; Li, T.; Xu, Y.; Liu, S.; Barmak, K.; Watanabe, K.; Taniguchi, T.; MacDonald, A. H.; Shan, J.; Mak, K. F. Simulation of Hubbard model physics in WSe 2/WS 2 moiré superlattices. *Nature* **2020**, *579* (7799), 353−358.

(11) Ulstrup, S.; Koch, R. J.; Singh, S.; McCreary, K. M.; Jonker, B. T.; Robinson, J. T.; Jozwiak, C.; Rotenberg, E.; Bostwick, A.; Katoch, J.; Miwa, J. A. Direct observation of minibands in a twisted graphene/WS2 bilayer. *Science advances* **2020**, *6* (14), eaay6104.

(12) Xu, Y.; Liu, S.; Rhodes, D. A.; Watanabe, K.; Taniguchi, T.; Hone, J.; Elser, V.; Mak, K. F.; Shan, J. Correlated insulating states at fractional fillings of moiré superlattices. *Nature* **2020**, *587* (7833), 214−218.

(13) Zhang, L.; Zhang, Z.; Wu, F.; Wang, D.; Gogna, R.; Hou, S.; Watanabe, K.; Taniguchi, T.; Kulkarni, K.; Kuo, T.; Forrest, S. R.; Deng, H. Twist-angle dependence of moiré excitons in WS 2/MoSe 2 heterobilayers. *Nat. Commun.* **2020**, *11* (1), 1−8.

(14) Zhang, L.; Deng, H. Flatland, lineland and dotland. *Nat. Mater.* **2020**, *19* (10), 1044−1045.

(15) Sung, J.; Zhou, Y.; Scuri, G.; Zolyomi, V.; Andersen, T. I.; Yoo, H.; Wild, D. S.; Joe, A. Y.; Gelly, R. J.; Heo, H.; Magorrian, S. J.; Berube, D.; Valdivia, A. M. M.; Taniguchi, T.; Watanabe, K.; Lukin, M. D.; Kim, P.; Fal'ko, V. I.; Park, H. Broken mirror symmetry in excitonic response of reconstructed domains in twisted MoSe2/MoSe2 bilayers. *Nat. Nanotechnol.* **2020**, *15* (9), 750−754.

(16) Sharpe, A. L.; Fox, E. J.; Barnard, A. W.; Finney, J.; Watanabe, K.; Taniguchi, T.; Kastner, M.; Goldhaber-Gordon, D. Emergent ferromagnetism near three-quarters filling in twisted bilayer graphene. *Science* **2019**, *365* (6453), 605−608.

(17) Chen, G.; Sharpe, A. L.; Fox, E. J.; Zhang, Y.-H.; Wang, S.; Jiang, L.; Lyu, B.; Li, H.; Watanabe, K.; Taniguchi, T.; Shi, Z.; Senthil, T.; Goldhaber-Gordon, D.; Zhang, Y.; Wang, F. Tunable correlated chern insulator and ferromagnetism in a moiré superlattice. *Nature* **2020**, *579* (7797), 56−61.

(18) Jin, C.; Regan, E. C.; Yan, A.; Iqbal Bakti Utama, M.; Wang, D.; Zhao, S.; Qin, Y.; Yang, S.; Zheng, Z.; Shi, S.; Watanabe, K.; Taniguchi, T.; Tongay, S.; Zettl, A.; Wang, F. Observation of moiré excitons in WSe 2/WS 2 heterostructure superlattices. *Nature* **2019**, *567* (7746), 76−80.

(19) Seyler, K. L.; Rivera, P.; Yu, H.; Wilson, N. P.; Ray, E. L.; Mandrus, D. G.; Yan, J.; Yao, W.; Xu, X. Signatures of moiré-trapped valley excitons in MoSe 2/WSe 2 heterobilayers. *Nature* **2019**, *567* (7746), 66−70.
(20) Tran, K.; Moody, G.; Wu, F.; Lu, X.; Choi, J.; Kim, K.; Rai, A.; Sanchez, D. A.; Quan, J.; Singh, A.; Embley, J.; Zepeda, A.; Campbell, M.; Autry, T.; Taniguchi, T.; Watanabe, K.; Lu, N.; Banerjee, S. K.; Silverman, K. L.; Kim, S.; Tutuc, E.; Yang, L.; MacDonald, A. H.; Li, X. Evidence for moiré excitons in van der Waals heterostructures. *Nature* **2019**, *567* (7746), 71−75.
(21) Yu, H.; Liu, G.-B.; Tang, J.; Xu, X.; Yao, W. Moiré excitons: From programmable quantum emitter arrays to spin-orbit−coupled artificial lattices. *Science advances* **2017**, *3* (11), e1701696.
(22) Zhang, N.; Surrente, A.; Baranowski, M.; Maude, D. K.; Gant, P.; Castellanos-Gomez, A.; Plochocka, P. Moiré intralayer excitons in a MoSe2/MoS2 heterostructure. *Nano Lett.* **2018**, *18* (12), 7651−7657.
(23) Andersen, T. I.; Scuri, G.; Sushko, A.; De Greve, K.; Sung, J.; Zhou, Y.; Wild, D. S.; Gelly, R. J.; Heo, H.; Berube, D.; Joe, A. Y.; Jauregui, L. A.; Watanabe, K.; Taniguchi, T.; Kim, P.; Park, H.; Lukin, M. D. Excitons in a reconstructed moiré potential in twisted WSe 2/WSe 2 homobilayers. *Nat. Mater.* **2021**, *20*, 1−8.
(24) Dou, X.; Ding, K.; Jiang, D.; Fan, X.; Sun, B. Probing spin−orbit coupling and interlayer coupling in atomically thin molybdenum disulfide using hydrostatic pressure. *ACS Nano* **2016**, *10* (1), 1619−1624.
(25) Dou, X.; Ding, K.; Jiang, D.; Sun, B. Tuning and identification of interband transitions in monolayer and bilayer molybdenum disulfide using hydrostatic pressure. *ACS Nano* **2014**, *8* (7), 7458−7464.
(26) Dybała, F.; Polak, M.; Kopaczek, J.; Scharoch, P.; Wu, K.; Tongay, S.; Kudrawiec, R. Pressure coefficients for direct optical transitions in MoS 2, MoSe 2, WS 2, and WSe 2 crystals and semiconductor to metal transitions. *Sci. Rep.* **2016**, *6*, 26663.
(27) Nayak, A. P.; Yuan, Z.; Cao, B.; Liu, J.; Wu, J.; Moran, S. T.; Li, T.; Akinwande, D.; Jin, C.; Lin, J.-F. Pressure-modulated conductivity, carrier density, and mobility of multilayered tungsten disulfide. *ACS Nano* **2015**, *9* (9), 9117−9123.
(28) Yan, Y.; Li, F.; Gong, Y.; Yao, M.; Huang, X.; Fu, X.; Han, B.; Zhou, Q.; Cui, T. Interlayer coupling affected structural stability in ultrathin MoS2: an investigation by high pressure Raman spectroscopy. The. *J. Phys. Chem. C* **2016**, *120* (43), 24992−24998.
(29) Yankowitz, M.; Jung, J.; Laksono, E.; Leconte, N.; Chittari, B. L.; Watanabe, K.; Taniguchi, T.; Adam, S.; Graf, D.; Dean, C. R. Dynamic band-structure tuning of graphene moiré superlattices with pressure. *Nature* **2018**, *557* (7705), 404−408.
(30) Lambelet, P.; Sayah, A.; Pfeffer, M.; Philipona, C.; Marquis-Weible, F. Chemically etched fiber tips for near-field optical microscopy: a process for smoother tips. *Appl. Opt.* **1998**, *37* (31), 7289−7292.
(31) Puygranier, B.; Dawson, P. Chemical etching of optical fibre tips—Experiment and model. *Ultramicroscopy* **2000**, *85* (4), 235−248.
(32) Karrai, K.; Grober, R. D. Piezoelectric tip-sample distance control for near field optical microscopes. *Appl. Phys. Lett.* **1995**, *66* (14), 1842−1844.
(33) Behme, G.; Richter, A.; Süptitz, M.; Lienau, C. Vacuum near-field scanning optical microscope for variable cryogenic temperatures. *Rev. Sci. Instrum.* **1997**, *68* (9), 3458−3463.
(34) Bao, W.; Borys, N. J.; Ko, C.; Suh, J.; Fan, W.; Thron, A.; Zhang, Y.; Buyanin, A.; Zhang, J.; Cabrini, S.; Ashby, P. D.; Weber-Bargioni, A.; Tongay, S.; Aloni, S.; Ogletree, D. F.; Wu, J.; Salmeron, M. B.; Schuck, P. J. Visualizing nanoscale excitonic relaxation properties of disordered edges and grain boundaries in monolayer molybdenum disulfide. *Nat. Commun.* **2015**, *6* (1), 1−7.
(35) Bao, W.; Melli, M.; Caselli, N.; Riboli, F.; Wiersma, D. S.; Staffaroni, M.; Choo, H.; Ogletree, D. F.; Aloni, S.; Bokor, J.; Cabrini, S.; Intonti, F.; Salmeron, M. B.; Yablonovitch, E.; Schuck, P. J.; Weber-Bargioni, A. Mapping local charge recombination heterogeneity by multidimensional nanospectroscopic imaging. *Science* **2012**, *338* (6112), 1317−1321.
(36) Sinogeikin, S. V.; Smith, J. S.; Rod, E.; Lin, C.; Kenney-Benson, C.; Shen, G. Online remote control systems for static and dynamic compression and decompression using diamond anvil cells. *Rev. Sci. Instrum.* **2015**, *86* (7), 072209.
(37) Mao, W. L.; Mao, H.-k. Ultrahigh-pressure experiment with a motor-driven diamond anvil cell. *J. Phys.: Condens. Matter* **2006**, *18* (25), S1069.
(38) Lee, G. W.; Evans, W. J.; Yoo, C.-S. Crystallization of water in a dynamic diamond-anvil cell: Evidence for ice VII-like local order in supercompressed water. *Phys. Rev. B: Condens. Matter Mater. Phys.* **2006**, *74* (13), 134112.
(39) Jin, C.; Regan, E. C.; Wang, D.; Iqbal Bakti Utama, M.; Yang, C.-S.; Cain, J.; Qin, Y.; Shen, Y.; Zheng, Z.; Watanabe, K.; Taniguchi, T.; Tongay, S.; Zettl, A.; Wang, F. Identification of spin, valley and moiré quasi-angular momentum of interlayer excitons. *Nat. Phys.* **2019**, *15* (11), 1140−1144.
(40) Wu, F.; Lovorn, T.; MacDonald, A. Theory of optical absorption by interlayer excitons in transition metal dichalcogenide heterobilayers. *Phys. Rev. B: Condens. Matter Mater. Phys.* **2018**, *97* (3), 035306.
(41) Shen, G.; Wang, Y.; Dewaele, A.; Wu, C.; Fratanduono, D. E.; Eggert, J.; Klotz, S.; Dziubek, K. F.; Loubeyre, P.; Fat'yanov, O. V.; Asimow, P. D.; Mashimo, T.; Wentzcovitch, R. M. M. Toward an international practical pressure scale: A proposal for an IPPS ruby gauge (IPPS-Ruby2020). *High Pressure Res.* **2020**, *40* (3), 299−314.
(42) Wu, F.; Lovorn, T.; MacDonald, A. H. Topological exciton bands in moiré heterojunctions. *Phys. Rev. Lett.* **2017**, *118* (14), 147401.

https://doi.org/10.1021/acs.nanolett.1c03611
Nano Lett. 2021, 21, 8910−8916